RSC Advances

PAPER

View Article Online
View Journal | View Issue

Cite this: *RSC Adv.*, 2019, **9**, 40437

Computational study on the mechanism and kinetics for the reaction between HO_2 and *n*-propyl peroxy radical†

Zhenli Yang,[ab] Xiaoxiao Lin,[*a] Jiacheng Zhou,[ab] Mingfeng Hu,[a] Yanbo Gai,[a] Weixiong Zhao,[a] Bo long[c] and Weijun Zhang[*ad]

Received 17th September 2019
Accepted 28th November 2019

DOI: 10.1039/c9ra07503h

rsc.li/rsc-advances

The *n*-propyl peroxy radical (*n*-$C_3H_7O_2$) is the key intermediate during atmospheric oxidation of propane (C_3H_8) which plays an important role in the carbon and nitrogen cycles in the troposphere. In this paper, a comprehensive theoretical study on the reaction mechanism and kinetics of the reaction between HO_2 and *n*-$C_3H_7O_2$ was performed at the CCSD(T)/aug-cc-pVDZ//B3LYP/6-311G(d,p) level of theory. Computational results show that the HO_2 + *n*-$C_3H_7O_2$ reaction proceeds on both singlet and triplet potential energy surfaces (PESs). From an energetic point of view, the formation of $C_3H_7O_2H$ and $^3O_2$ *via* triplet hydrogen abstraction is the most favorable channel while other product channels are negligible. In addition, the calculated rate constants for the title reaction over the temperature range of 238–398 K were calculated by the multiconformer transition state theory (MC-TST), and the calculated rate constants show a negative temperature dependence. The contributions of the other four reaction channels to the total rate constant are negligible.

1. Introduction

Propane (C_3H_8) is one of the most important nonmethane hydrocarbons (NMHCs) with a lifetime of about 14 days and its global emissions are estimated to be 15–20 Tg per year.[1,2] For decades, propane oxidation has been of great interest, and the *n*-propyl peroxy radical (*n*-$C_3H_7O_2$) is one of the key intermediates during propane oxidation.[3–6]

$$CH_3CH_2CH_3 \xrightarrow{OH \text{ or } Cl} CH_3CH_2\dot{C}H_2 \quad n\text{-propyl radical} \quad (1)$$

$$CH_3CH_2\dot{C}H_2 \xrightarrow{O_2} CH_3CH_2CH_2O_2^{\cdot} \quad n\text{-propyl peroxy radical} \quad (2)$$

In clean environments where NO_x concentrations are low, the reactions of HO_2 with organic peroxy radicals (RO_2) are generally considered as an important sink.[7–11] The reaction mechanisms and kinetic data of HO_2 + RO_2 reactions have not yet been well-established mainly because of inherent problems in exploring radical–radical reactions.[12] Besides, to the best of our knowledge, only a few studies for both kinetics and mechanism of the HO_2 + *n*-$C_3H_7O_2$ reaction have been reported. One of the difficulties is that the *n*-$C_3H_7O_2$ radical is more complex than CH_3O_2 and $C_2H_5O_2$ due to its rich conformational variety. It has been reported that the *n*-$C_3H_7O_2$ radical has five different conformers: G_1G_2, G_1T_2, $G_1'G_2$, T_1G_2 and T_1T_2 (see Fig. S1 in the ESI†).[13–15]

Hou and co-workers have developed a structure–activity relationships (SAR) model to study structure–activity relationships and the characteristics of the HO_2 + RO_2 reactions.[10] They reported the calculated rate constant for HO_2 + $C_3H_7O_2$ reaction as 9.12×10^{-12} cm^3 per molecule per s. However, the detailed reaction mechanism and kinetic data of HO_2 + *n*-$C_3H_7O_2$ reaction are still unclear. To better understanding of this issue, a systematic theoretical investigation on the HO_2 + *n*-$C_3H_7O_2$ reaction is required. In this work, quantum chemistry calculations have been performed to explore the detailed reaction mechanism of HO_2 + *n*-$C_3H_7O_2$ reaction both on the singlet and triplet potential energy surfaces. Then the rate constant of the title reaction was calculated using the multiconformer transition state theory (MC-TST) which considered that the *n*-$C_3H_7O_2$ radical has multiple conformers.

2. Computational methods

The geometries of the reactants, intermediates, transitions states and products in the HO_2 + *n*-$C_3H_7O_2$ reaction were fully

[a]*Laboratory of Atmospheric Physico-Chemistry, Anhui Institute of Optics and Fine Mechanics, Chinese Academy of Sciences, Hefei, 230031, Anhui, China. E-mail: wjzhang@aiofm.ac.cn; lxx1989@aiofm.ac.cn*

[b]*University of Science and Technology of China, Hefei 230026, China*

[c]*College of Computer and Information Engineering, Guizhou Minzu University, Guiyang 550025, China*

[d]*School of Environmental Science and Optoelectronic Technology, University of Science and Technology of China, Hefei, 230026, Anhui, China*

† Electronic supplementary information (ESI) available. See DOI: 10.1039/c9ra07503h

optimized by Density Functional Theory (DFT) method at the B3LYP/6-311G(d,p) level of theory.[16,17] Harmonic vibrational frequencies were calculated at the same level to confirm that all minima are real frequencies, and transition states have only a single imaginary frequency. Vibrational frequencies and coordinates of all stationary points in the title reaction have been summarized Tables S1 and S2,† respectively (see ESI†). In addition, the intrinsic reaction coordinate (IRC) calculations were also carried out to verify that the transition states structures can be connected to the corresponding reactants and products.[18–21] The zero-point energies (ZPEs) and the thermodynamic corrections at the temperature of 298.15 K and pressure of 1 atm were evaluated at the B3LYP/6-311G(d,p) level of theory and were incorporated in to the final energy barrier, enthalpy and Gibbs free energy. To get more reliable energy information, single point energy calculations were carried out at CCSD(T)/aug-cc-pVDZ level of theory.[22] In CCSD (T) calculation, T_1 diagnostic is thought to assess the reliability of the methods with respect to a possible multireference feature of the wave functions. For open-shell systems, if the T_1 diagnostic value do not exceed 0.044, the wave functions of CCSD are considered to be reliable.[23–26] The T_1 diagnostic values of the stationary points are presented in Table S3 (ESI†). T1 diagnostic values of the stationary points except for G_1G_2-^{3}TS1, G_1T_2-^{3}TS1, G'_1G_2-^{3}TS1 are less than 0.044 from Table S3,† revealing that the CCSD wave function could be reliable. All the computations were performed with Gaussian 09 program package.[27] The CCSD(T) single point energy computations were carried out by Molpro package.[28,29]

Since that the n-$C_3H_7O_2$ has multiple conformers, such complexity should be taken account into the rate constant formula, multiconformer transition state theory (MC-TST) method were carried out for rate constant calculations.[30–33] Within the framework of the conventional transition state theory (TST),[34–36] the MC-TST expression for a rate constant k at temperature T can be written as

$$k_{\text{MC-TST}} = \kappa \frac{k_B T}{h} \frac{\sum_{i}^{\text{all TS conf.}} \exp\left(\frac{-\Delta E_i}{k_B T}\right) Q_{\text{TS},i}}{\sum_{j}^{\text{all R conf.}} \exp\left(\frac{-\Delta E_j}{k_B T}\right) Q_{\text{R},j}} \times \exp\left(-\frac{E_{\text{TS},0} - E_{\text{R},0}}{k_B T}\right) \quad (3)$$

Here κ is the Eckart tunneling correction[37] factor associated with the lowest energy transition state. k_B and h are Boltzmann's constant and Planck's constant, respectively. ΔE_i represents the difference in zero-point corrected energy between the transition state conformer i and the lowest energy transition state conformer, and $Q_{\text{TS},i}$ represents the total partition function of the transition state conformer i. ΔE_j denotes zero-point corrected energy of reactant conformer j relative to the lowest energy reactant conformer, and $Q_{\text{R},j}$ represents the partition function of reactant conformer j. $E_{\text{TS},0}$ and $E_{\text{R},0}$ represent the zero-point corrected energy of the lowest energy conformer of the transition state and reactant, respectively. The energies in the MC-TST expression were computed at the CCSD(T)/aug-cc-pVDZ//B3LYP/6-311G(d,p) level of theory and the partition functions were obtained at the B3LYP/6-311G(d,p) level of theory.

3. Results and discussion

The scheme of the possible reaction routes for the HO_2 + n-$C_3H_7O_2$ reaction has been showed in Fig. 1. In this section, the reaction mechanism and kinetics of the HO_2 + n-$C_3H_7O_2$ reaction have been discussed. For simplicity, we first focus on the reaction mechanism of HO_2 and the most stable G_1G_2 conformer reaction in the following parts. The HO_2 + G_1T_2, G'_1G_2, T_1G_2 and T_1T_2 reactions are compared with the HO_2 + G_1G_2 reaction. The schematic energy diagram of the HO_2 + G_1G_2 reaction is depicted in Fig. 2, whereas the corresponding profiles of the schematic energy diagram are shown schematically in Fig. S2–S5† for the HO_2 + G_1T_2, G'_1G_2, T_1G_2 and T_1T_2 reactions (ESI†), respectively. The selected geometric structures of the five reactions are displayed in Fig. 3 and S6–S9,† respectively. In what follows, energies of the HO_2 + G_1G_2, G_1T_2, G'_1G_2, T_1G_2 and T_1T_2 reactions are shown in Tables 1 and S4–S7,† respectively. Besides, to study the relative importance of various products in the HO_2 + n-$C_3H_7O_2$, the rate constants of the most favorable channel for the five different reactions have been discussed. Finally, Arrhenius plot for the triplet channel of HO_2 + n-$C_3H_7O_2$ reaction is displayed in Fig. 4 and the calculated rate constants are fitted into Arrhenius three parameter equation.

Throughout the discussions, the transition states and intermediates in each reaction are denoted by "TS'' and "IM", respectively, followed by a number. The optimized geometries involved in the five reactions are designated by the prefix G_1G_2, G_1T_2, G'_1G_2, T_1G_2 and T_1T_2, respectively, followed by the "TS'' or "IM".

3.1 Mechanism of the HO_2 + n-$C_3H_7O_2$ reaction

3.1.1 Reaction mechanism on triplet PES. A schematic presentation of triplet potential energy surfaces for the reaction between HO_2 and individual n-$C_3H_7O_2$ conformer have been computed at the CCSD(T)/aug-cc-pVDZ//B3LYP/6-311G(d,p) level of theory. For example, in the case of the HO_2 and G_1G_2 conformer reaction, schematic energy diagram of the reaction is shown in Fig. 2 and the geometric structures of reactants, intermediates, transition states and products are depicted in Fig. 3. For the triplet potential energy surface, our calculations show one possible reaction pathway proceeding through a pre-

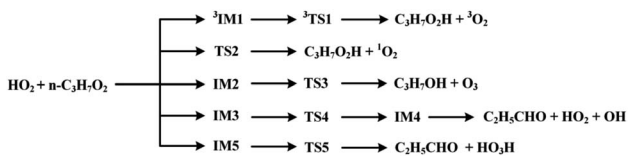

Fig. 1 The scheme of possible reaction routes of HO_2 + n-$C_3H_7O_2$ reaction on both the singlet and triplet potential energy surfaces.

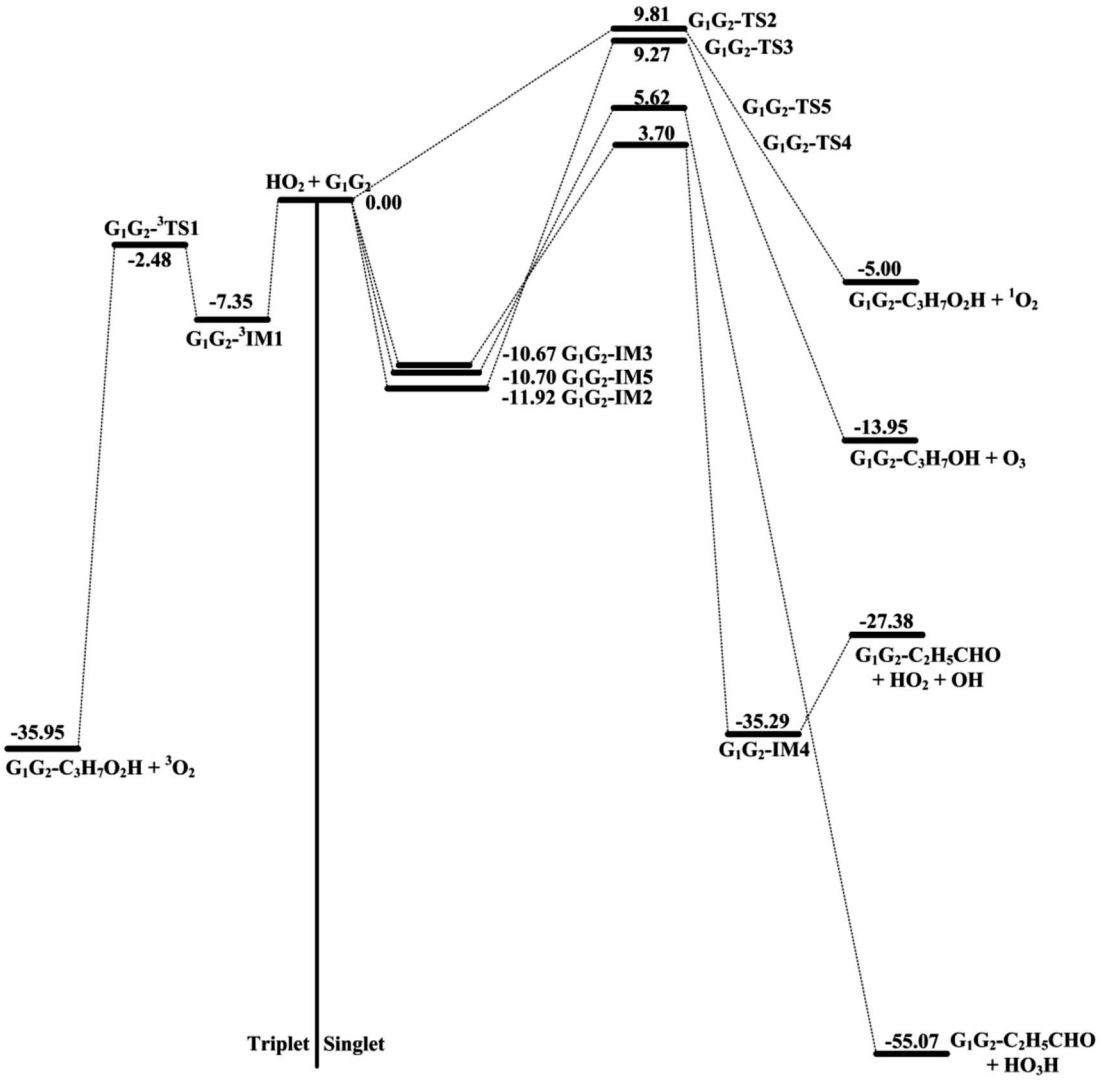

Fig. 2 Schematic energy diagram of HO_2 + G_1G_2 reaction computed at the CCSD(T)/aug-cc-pVDZ//B3LYP/6-311G(d,p) level of theory on both the singlet and triplet potential energy surfaces. Energies are in units of kcal mol^{-1}.

reaction complex G_1G_2-^{3}IM1 and a transition state G_1G_2-^{3}TS1 to produce G_1G_2-$C_3H_7O_2H$ and triplet O_2. This pathway is a hydrogen abstraction process by the H atom on the HO_2 radical migrates to the terminal oxygen of G_1G_2. In G_1G_2-^{3}IM1, the length of hydrogen bond between the terminal oxygen atom of G_1G_2 and the hydrogen atom of HO_2 is 1.801 Å, which is 0.408 Å longer than that in the G_1G_2-^{3}TS1. It is stabilized by the hydrogen bond interaction with a binding energy of −7.35 kcal mol^{-1} relative to the HO_2 + G_1G_2 reactants. From the equilibrium structure of G_1G_2-^{3}TS1 shown in Fig. 3, the breaking H–O and the forming O–H bonds are 1.064 and 1.393 Å, respectively. The breaking H–O bond is only slightly longer by 0.089 Å compared to the equilibrium of H–O bond in HO_2 radical. The O···H···O bond angle is nearly linear with a value of approximately 171.93°. The barrier of G_1G_2-^{3}TS1 is −2.48 kcal mol^{-1}. G_1G_2-^{3}TS1 is an early barrier compared to other different channels in the reaction of HO_2 + G_1G_2.

For the triplet hydrogen abstraction process, the HO_2 + G_1T_2, G'_1G_2, T_1G_2 and T_1T_2 four reactions are also identified to be kinetically favorable pathways *via* the same reaction mechanism as that of HO_2 + G_1G_2 reaction (see Fig. S2–S5†). The selected geometric structures for the reactants, intermediates, transition states and products of the four reactions were shown in Fig. S6–S9,† respectively. As shown in Fig. S2–S5,† all the four reactions take place on the triplet surfaces from the reactants *via* intermediates (G_1T_2-^{3}IM1, G'_1G_2-^{3}IM1, T_1G_2-^{3}IM1 and T_1T_2-^{3}IM1) and transition states (G_1T_2-^{3}TS1, G'_1G_2-^{3}TS1, T_1G_2-^{3}TS1 and T_1T_2-^{3}TS1) to produce the $C_3H_7O_2H$ and triplet O_2. The four intermediates are hydrogen bond complexes. The binding energies of four intermediates are −6.83 kcal mol^{-1} (G_1T_2-^{3}IM1), −6.73 kcal mol^{-1} (G'_1G_2-^{3}IM1), −6.81 kcal mol^{-1} (T_1G_2-^{3}IM1) and −6.79 kcal mol^{-1} (T_1T_2-^{3}IM1) kcal mol^{-1}, respectively. In the structure of G_1G_2-^{3}IM1, the binding energy is −7.35 kcal mol^{-1}, which is close to that in the four intermediates above. The four corresponding transition states involve

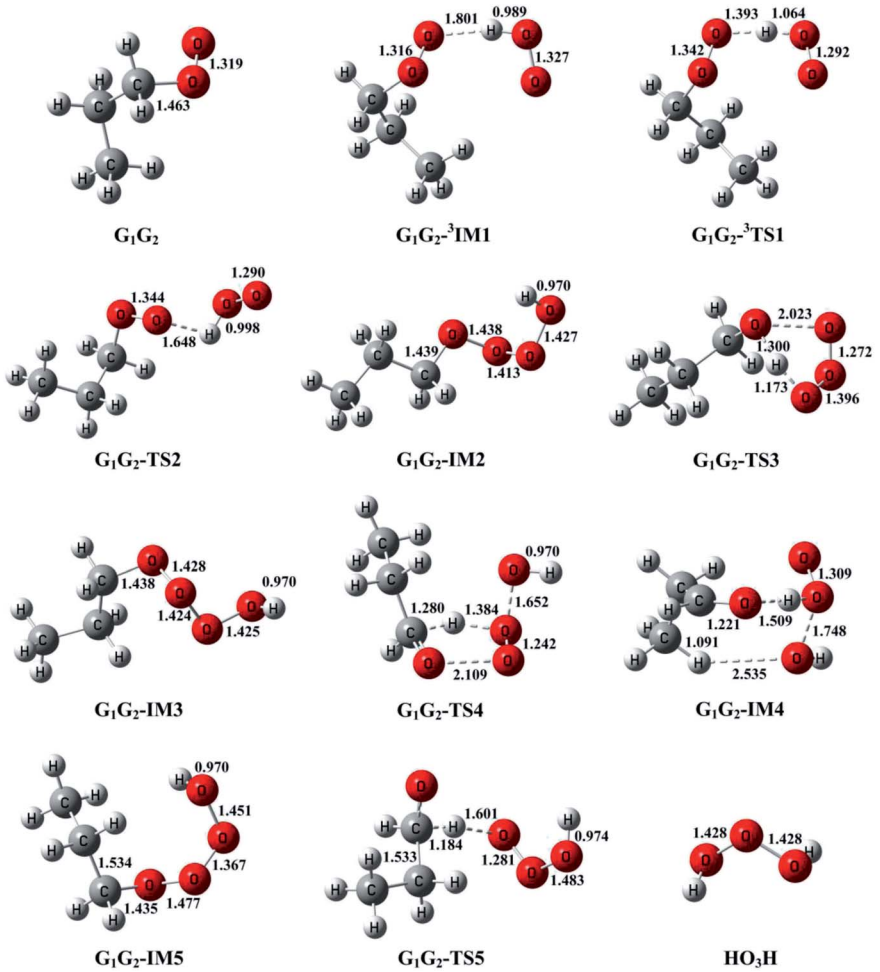

Fig. 3 Selected geometric structures of the reactants, intermediates and transition states of HO_2 + G_1G_2 reaction computed at the B3LYP/6-311G(d,p) level of theory on both the singlet and triplet potential energy surfaces. Bond distances are given in angstroms.

Table 1 Zero point energies (ZPE), relative energies ($\Delta E_{298\ K}$), reaction enthalpies ($\Delta H_{298\ K}$) and Gibbs free energies ($\Delta G_{298\ K}$) of the stationary points involved in HO_2 + G_1G_2 reaction. Energies are computed at the CCSD(T)/aug-cc-pVDZ//B3LYP/6-311G(d,p) level of theory. Energy values are given in kcal mol^{-1}

Compound	ZPE	$\Delta E_{298\ K}$	$\Delta H_{298\ K}$	$\Delta G_{298\ K}$
G_1G_2 + HO_2	71.62	0.00	0.00	0.00
G_1G_2-^{3}IM1	73.23	−6.78	−7.37	1.82
G_1G_2-^{3}TS1	70.85	−2.47	−3.06	7.59
G_1G_2-$C_3H_7O_2H$ + $^3O_2$	72.27	−35.88	−35.88	−34.48
G_1G_2-TS2	72.41	9.96	9.36	20.45
G_1G_2-$C_3H_7O_2H$ + $^1O_2$	72.25	−4.93	−4.93	−2.88
G_1G_2-IM2	74.18	−12.02	−12.61	−0.41
G_1G_2-TS3	71.22	8.76	8.17	21.28
G_1G_2-C_3H_7OH + O_3	72.58	−14.26	−14.26	−13.41
G_1G_2-IM3	73.98	−10.77	−11.36	0.85
G_1G_2-TS4	69.91	3.58	2.99	15.51
G_1G_2-IM4	72.52	−34.70	−35.29	−24.64
G_1G_2-C_2H_5CHO + HO_2 + OH	66.88	−26.53	−25.94	−36.40
G_1G_2-IM5	74.07	−10.94	−11.53	1.28
G_1G_2-TS5	68.74	6.10	5.51	15.13
G_1G_2-C_2H_5CHO + HO_3H	71.73	−55.18	−55.18	−54.90

nearly linear O···H···O bond angles and are early barriers. The average distances of the breaking H–O bonds and forming O–H bonds are 1.041 and 1.466 Å, respectively. The barrier heights of

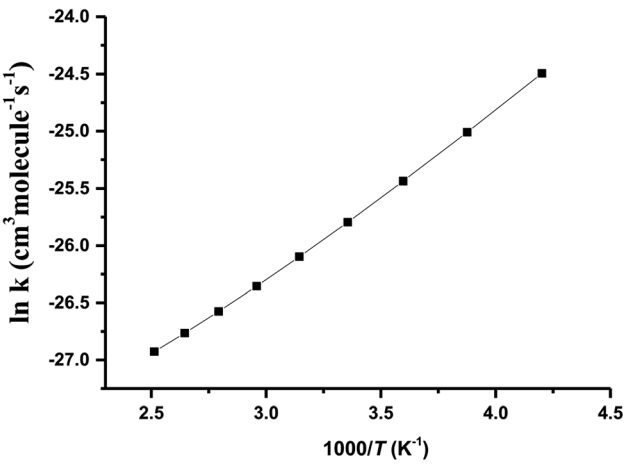

Fig. 4 Arrhenius plot of calculated rate coefficients for G_1G_2-$C_3H_7O_2H$ + $^3O_2$ formation in HO_2 + n-$C_3H_7O_2$ reaction within the temperature range of 238–398 K at the CCSD(T)/aug-cc-pVDZ//B3LYP/6-311G(d,p) level of theory.

the G_1T_2-^{3}TS1, G'_1G_2-^{3}TS1, T_1G_2-^{3}TS1 and T_1T_2-^{3}TS1 are close to each other (−3.26, −2.15, −3.85 *vs.* −3.90 kcal mol^{-1}). The average barrier height of the four transition states is −3.29 kcal mol^{-1}, which is only 0.81 kcal mol^{-1} lower than G_1G_2-^{3}TS1. Evidently, G_1G_2-^{3}TS1, G_1T_2-^{3}TS1, G'_1G_2-^{3}TS1, T_1G_2-^{3}TS1 and T_1T_2-^{3}TS1 are all early barriers. The reactions of HO_2 with the five different conformers (G_1G_2, G_1T_2, G'_1G_2, T_1G_2 and T_1T_2) have same reaction mechanism and have simpler triplet potential energy surfaces *via* hydrogen abstraction routes to form $C_3H_7O_2H$ + $^3O_2$ molecule.

3.1.2 Reaction mechanism on singlet PES. It can be seen in Fig. 2, the HO_2 + G_1G_2 reaction has a more complicated singlet potential energy surface. In singlet reaction, there are four different reaction pathways in where products are G_1G_2-$C_3H_7O_2H$ + $^1O_2$, G_1G_2-C_3H_7OH + O_3, G_1G_2-C_2H_5CHO + HO_2 + OH and G_1G_2-C_2H_5CHO + HO_3H. The detailed reaction mechanisms of the HO_2 + G_1G_2 reaction are discussed in the following parts.

The formation of G_1G_2-$C_3H_7O_2H$ + $^1O_2$ proceeds directly through one transition state G_1G_2-TS2 by abstracting the hydrogen atom of HO_2 to the terminal O atom of G_1G_2, which has been shown in Fig. 2. The barrier height of G_1G_2-TS2 is calculated to be 9.81 kcal mol^{-1} higher than that of the initial HO_2 + G_1G_2 reactants. This product channel is a hydrogen abstraction process, which is different from the hydrogen abstraction on the triplet surface. In summary, the singlet hydrogen abstraction process is distinct from the triplet one in three respects. Firstly, hydrogen abstraction process on the singlet potential energy surface may undergo directly through the transition state G_1G_2-TS2 producing G_1G_2-$C_3H_7O_2H$ and singlet O_2 molecule, while the triplet one proceeds the intermediate G_1G_2-^{3}IM1 prior to the transition state G_1G_2-^{3}TS1 producing G_1G_2-$C_3H_7O_2H$ and triplet O_2 molecule. Secondly, the O···H···O bond angle in G_1G_2-TS2 is much more bent (*i.e.*, 107.77° in G_1G_2-TS2 *vs.* 171.93° in G_1G_2-^{3}TS1). Thirdly, our calculation shows the barrier for G_1G_2-TS2 is much higher than that for G_1G_2-^{3}TS1 by about 12.29 kcal mol^{-1}. The G_1G_2-$C_3H_7O_2H$ + $^1O_2$ formation channel is of minor importance due to the high barrier height.

On the singlet potential energy surface, except for direct hydrogen abstraction mechanism described above, addition–elimination mechanism is located as well. The remaining three reaction pathways precede *via* an addition–elimination mechanism. As shown in Fig. 2, HO_2 + G_1G_2 → G_1G_2-IM2 → G_1G_2-TS3 → G_1G_2-C_3H_7OH + O_3, this channel involves a rather high barrier and is exothermic. The structures of G_1G_2-IM2 and G_1G_2-TS3 are shown in Fig. 3. The lengths of three O–O bonds of G_1G_2-IM2 are about 1.4 Å. G_1G_2-IM2 is −11.92 kcal mol^{-1} with respect to the initial HO_2 + G_1G_2 reactants. G_1G_2-TS3 is a five-membered ring structure. With respect to the HO_2 + G_1G_2 reactants, the barrier of G_1G_2-TS3 is as high as 9.27 kcal mol^{-1}. Compared with other pathways, the formations of G_1G_2-C_3H_7OH + O_3 might be negligible because of the high barrier height.

The formation of G_1G_2-TS4 from the reactants HO_2 + G_1G_2 radicals could also occur *via* G_1G_2-IM3. Similar to G_1G_2-IM2, G_1G_2-IM3 also has three OO bonds and the bond lengths are about 1.4 Å. The computed binding energy for G_1G_2-IM3 are −10.67 kcal mol^{-1}. In G_1G_2-TS4, the hydrogen atom migrates from the C to O to form HO_2, while the two O–O bonds cleavage to form post-reaction complex G_1G_2-IM4. The barrier for G_1G_2-TS4 is relatively higher than that for G_1G_2-^{3}TS1 by about 6.18 kcal mol^{-1}. After G_1G_2-TS4, this product channel proceeds through G_1G_2-IM4 complex to form G_1G_2-C_2H_5CHO + HO_2 + OH products. It is found that the calculated relative energy of the G_1G_2-IM4 to the reactants HO_2 + G_1G_2 is −35.29 kcal mol^{-1}, which is lower than the products. It's worth noting that the reaction pathway of G_1G_2-C_2H_5CHO + HO_2 + OH formation could be viewed as a HO_2-mediated dissociation process of G_1G_2 because the HO_2 radical is also reproduced in the final products.

The last channel examined on the singlet potential energy surface is the formation of G_1G_2-C_2H_5CHO and HO_3H. As shown in Fig. 2, HO_2 + G_1G_2→ G_1G_2-IM5 → G_1G_2-TS5 →G_1G_2-C_2H_5CHO + HO_3H, this pathway involves a high barrier and is extremely exothermic. Analogous to the energies of G_1G_2-IM2 and G_1G_2-IM3, the binding energy for G_1G_2-IM5 is −10.70 kcal mol^{-1}. G_1G_2-IM5 also has three OO bonds, all of which are about 1.4 Å in length. The barrier height for G_1G_2-TS5 is about 5.62 kcal mol^{-1} with respect to the reactants HO_2 + G_1G_2. Clearly, the formation of G_1G_2-C_2H_5CHO and HO_3H *via* G_1G_2-TS5 involves significant barrier and is the most exothermic pathway on the both triplet and singlet potential energy surfaces.

From the Fig. S2–S5 in the ESI,† we can see that the singlet potential energy surfaces for the HO_2 + G_1T_2, G'_1G_2, T_1G_2 and T_1T_2 four reactions, as well as the HO_2 + G_1G_2 reaction proceed on the similar reaction mechanism which has been discussed above in detail in the present work. The formations of $C_3H_7O_2H$ + $^1O_2$, C_3H_7OH + O_3 and C_2H_5CHO + HO_2 + OH in HO_2 + G_1T_2, G'_1G_2, T_1G_2 and T_1T_2 four reactions have similar energetic data as that of the HO_2 + G_1G_2 reaction. For example, in the $C_3H_7O_2H$ + $^1O_2$ formation pathway, the barrier heights of the four transition states G_1T_2-TS2, G'_1G_2-^{3}TS2, T_1G_2-TS2 and T_1T_2-TS2 are generally consistent with each other (9.82, 9.51, 9.53 *vs.* 9.52 kcal mol^{-1}). The calculated barrier height for G_1G_2-TS2 is about 9.81 kcal mol^{-1}. By comparison, we can conclude that the energy barriers of the above three channels in the five reactions of HO_2 + G_1G_2, G_1T_2,G'_1G_2, T_1G_2 and T_1T_2 have little difference. However, in the C_2H_5CHO and HO_3H formation pathways, the average barrier height for the four transition states (G_1T_2-TS5, G'_1G_2-TS5, T_1G_2-TS5 and T_1T_2-TS5) is 14.80 kcal mol^{-1}, which is 9.18 kcal mol^{-1} higher than G_1G_2-TS5. As a result, for HO_2 + G_1G_2 reaction, the $C_3H_7O_2H$ + $^1O_2$ formation pathway is the highest barrier height, while C_2H_5CHO and HO_3H formation pathways are the highest barrier heights in the other four reactions. Compared with the energetically favorable triplet reactions, all the singlet reactions involve relatively high barriers.

In summary, the reactions of HO_2 with the five different conformers (G_1G_2, G_1T_2, G'_1G_2, T_1G_2 and T_1T_2) have simpler triplet potential energy surfaces *via* hydrogen abstraction routes to form $C_3H_7O_2H$ + $^3O_2$ molecule and more complicated singlet surfaces *via* direct hydrogen abstraction and addition–

elimination mechanisms form various products. From the mechanism discussed above, we can conclude that the pathway of formation of $C_3H_7O_2H$ + $^3O_2$ is the most important reaction channel and other channels can be negligible in the *n*-$C_3H_7O_2$ + HO_2 reaction.

3.2 Kinetics of the HO_2 + *n*-$C_3H_7O_2$reaction

Based on the singlet and triplet potential energy surfaces, the rate constants of different reaction pathways for the individual conformer have been evaluated using the conventional transition-state theory (TST) over the temperature range of 238–398 K. For example, in the case of the lowest energy conformer HO_2 + G_1G_2 reaction, the calculated rate constants for individual channel are listed in Table 2. As can be seen from Table 2, results show that the rate constants for the triplet hydrogen abstraction reaction contributes significantly to the overall rate constants. The rate constant of triplet channel is at least four orders of magnitude higher than that of singlet ones over the temperature range. This indicates that the triplet hydrogen abstraction channel for formation of G_1G_2-$C_3H_7O_2H$ + $^3O_2$ products is the major channel, while the singlet channels can be negligible. The reactions of HO_2 with the other conformers (G_1T_2, $G_1'G_2$, T_1G_2 and T_1T_2) have similar reaction mechanism and kinetic behavior as the HO_2 + G_1G_2 reaction. Thus, only the rate constants of each individual triplet hydrogen abstraction channel are considered in the total rate constants calculations of the HO_2 + *n*-$C_3H_7O_2$ reaction. The triplet channels for each *n*-$C_3H_7O_2$ conformer are displayed in Table 3. It is clear that rate constants for each triplet hydrogen abstraction channel give the total rate constants for the HO_2 + *n*-$C_3H_7O_2$ reaction. Considering that *n*-$C_3H_7O_2$ has multiple conformers, the total rate constants for HO_2 with *n*-$C_3H_7O_2$ reaction are obtained by MC-TST method. Overview of triplet channels for the reactions of HO_2 with the five conformers (G_1G_2, G_1T_2, $G_1'G_2$, T_1G_2 and T_1T_2) showing the individual conformer of the reactants, intermediates, transition states, and products are shown in the Fig. 5. The MC-TST rate constant can be regarded as a sum of the individual TST reaction rate constants which weighted by the Boltzmann population of the corresponding *n*-$C_3H_7O_2$ conformers. The overall calculated rate constant of the HO_2 + *n*-$C_3H_7O_2$ reaction over the temperature range of 238–398 K are listed in Table 4. Moreover, the calculated rate constants are fitted into Arrhenius three parameter equation as follows:

$$k = 3.97 \times 10^{-15}\left(\frac{T}{300}\right)^{2.49}\exp\left(\frac{2200}{T}\right) \quad (4)$$

The Arrhenius plot for the reaction of HO_2 and *n*-$C_3H_7O_2$ is shown in Fig. 4. From the Arrhenius plot, it can be seen clearly that the negative temperature dependence for the title reaction in lower temperature regime (*e.g.* T < 400 K). This can be

Table 2 Theoretical rate coefficients (cm^3 per molecule per s) for HO_2 + G_1G_2 reaction within the temperature range of 238–398 K at the CCSD(T)/aug-cc-pVDZ//B3LYP/6-311G(d,p) level of theory. $^3O_2$, $^1O_2$, O_3, OH and HO_3H denote the rate constant of product channel G_1G_2-$C_3H_7O_2H$ + $^3O_2$, G_1G_2-$C_3H_7O_2H$ + $^1O_2$, G_1G_2-C_3H_7OH + O_3, G_1G_2-C_2H_5CHO + HO_2 + OH and G_1G_2-C_2H_5CHO + HO_3H for the reaction, respectively

T (K)	$^3O_2$	$^1O_2$	O_3	OH	HO_3H
238	3.44×10^{-12}	4.70×10^{-24}	9.71×10^{-22}	6.18×10^{-19}	2.57×10^{-19}
258	2.22×10^{-12}	2.43×10^{-23}	8.96×10^{-22}	9.85×10^{-19}	6.70×10^{-19}
278	1.56×10^{-12}	1.01×10^{-22}	1.08×10^{-21}	1.52×10^{-18}	1.56×10^{-18}
298	1.16×10^{-12}	3.49×10^{-22}	1.52×10^{-21}	2.27×10^{-18}	3.30×10^{-18}
318	9.13×10^{-13}	1.05×10^{-21}	2.35×10^{-21}	3.28×10^{-18}	6.47×10^{-18}
338	7.45×10^{-13}	2.79×10^{-21}	3.78×10^{-21}	4.62×10^{-18}	1.19×10^{-17}
358	6.27×10^{-13}	6.73×10^{-21}	6.14×10^{-21}	6.35×10^{-18}	2.07×10^{-17}
378	5.42×10^{-13}	1.49×10^{-20}	9.91×10^{-21}	8.53×10^{-18}	3.43×10^{-17}
398	4.80×10^{-13}	3.06×10^{-20}	1.57×10^{-20}	1.12×10^{-17}	5.47×10^{-17}

Table 3 Theoretical rate coefficients (cm^3 per molecule per s) of the triplet channel for the five reactions within the temperature range of 238–398 K at the CCSD(T)/aug-cc-pVDZ//B3LYP/6-311G(d,p) level of theory

T (K)	HO_2 + G_1G_2	HO_2 + G_1T_2	HO_2 + $G_1'G_2$	HO_2 + T_1G_2	HO_2 + T_1T_2
238	3.44×10^{-12}	1.05×10^{-11}	1.12×10^{-12}	2.83×10^{-11}	4.61×10^{-11}
258	2.22×10^{-12}	6.30×10^{-12}	8.27×10^{-13}	1.57×10^{-11}	2.53×10^{-11}
278	1.56×10^{-12}	4.11×10^{-12}	6.45×10^{-13}	9.57×10^{-12}	1.53×10^{-11}
298	1.16×10^{-12}	2.87×10^{-12}	5.27×10^{-13}	6.31×10^{-12}	1.00×10^{-11}
318	9.13×10^{-13}	2.12×10^{-12}	4.45×10^{-13}	4.42×10^{-12}	7.00×10^{-12}
338	7.44×10^{-13}	1.64×10^{-12}	3.87×10^{-13}	3.26×10^{-12}	5.14×10^{-12}
358	6.27×10^{-13}	1.31×10^{-12}	3.44×10^{-13}	2.50×10^{-12}	3.93×10^{-12}
378	5.42×10^{-13}	1.08×10^{-12}	3.12×10^{-13}	1.99×10^{-12}	3.11×10^{-12}
398	4.80×10^{-13}	9.19×10^{-13}	2.88×10^{-13}	1.63×10^{-12}	2.54×10^{-12}

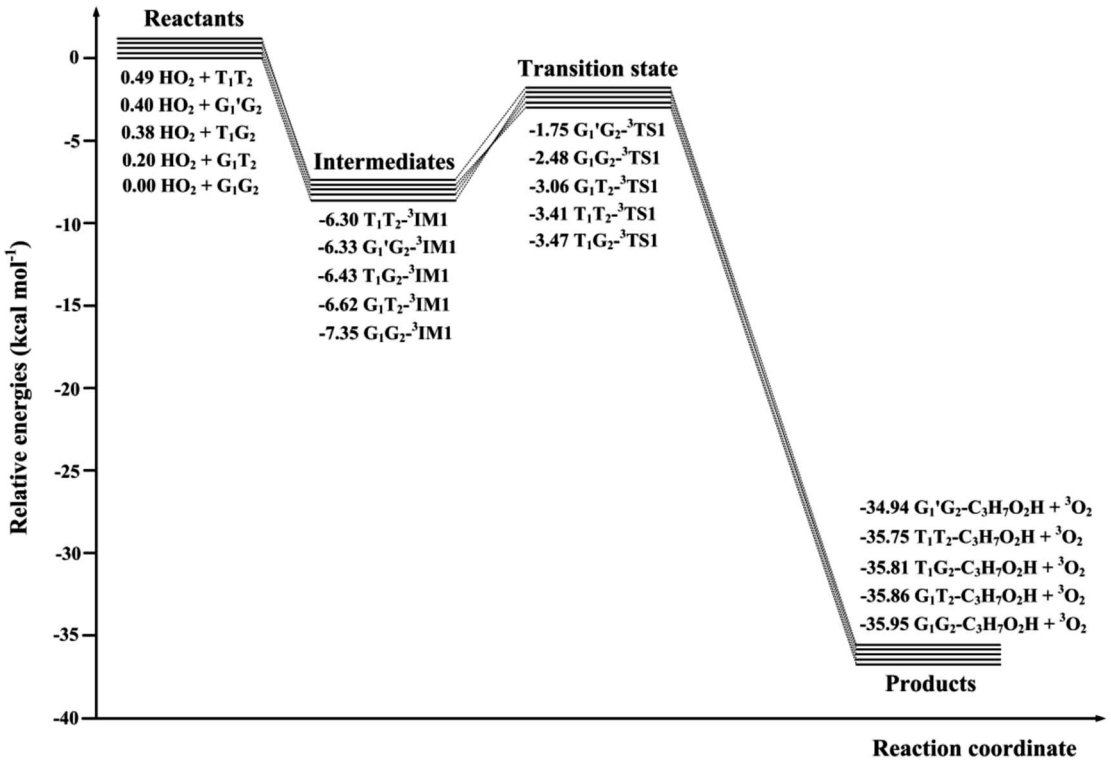

Fig. 5 In the multiconformer system, diagram showing triplet channels for the reactions of HO_2 radical with the five conformers (G_1G_2, G_1T_2, $G_1'G_2$, T_1G_2 and T_1T_2). All the energies ($\Delta(E + ZPE)$) are relative to the energies of $HO_2 + G_1G_2$.

attributed to the formation of the pre-reaction complexes with negative barriers in the triplet channels of the title reaction. For example, in the triplet channel of $HO_2 + G_1G_2$ reaction, the values of the rate coefficients of reverse process (G_1G_2-^{3}IM1 to HO_2 and G_1G_2) increases with the rising temperature, which reduces the value of the equilibrium constant. It can be said that when the reaction reaches equilibrium, the macroscopic rate coefficient decreases. This downward trend can be seen in the other four reactions of HO_2 with the different conformers (G_1T_2, $G_1'G_2$, T_1G_2 and T_1T_2). Thus, the overall rate coefficient of the title reaction shows negative temperature dependence. The calculated rate constants for $HO_2 + n$-$C_3H_7O_2$ reaction is predicted to be 6.27×10^{-12} cm^3 per molecule per s at 298 K. The kinetic results shown good agreement with the value 9.12×10^{-12} cm^3 per molecule per s reported by Hou and his co-workers using structure–activity relationships (SAR) analysis.[10] It shows that our CCSD(T)/aug-cc-pVDZ//B3LYP/6-311G(d,p) calculated rate constants are in good agreement with the available recent theoretical result in the related reference.

Table 4 The overall rate constants (cm^3 per molecule per s) within the temperature range 238–398 K for the $HO_2 + n$-$C_3H_7O_2$ reaction at CCSD(T)/aug-cc-pVDZ//B3LYP/6-311G(d,p) level of theory

T (K)	k_{total}
238	2.30×10^{-11}
258	1.38×10^{-11}
278	8.98×10^{-12}
298	6.27×10^{-12}
318	4.64×10^{-12}
338	3.58×10^{-12}
358	2.88×10^{-12}
378	2.38×10^{-12}
398	2.02×10^{-12}

4. Summary and conclusions

In present study, the detailed mechanism and kinetics of the reaction of HO_2 and n-$C_3H_7O_2$ (including five conformers G_1G_2, G_1T_2, $G_1'G_2$, T_1G_2 and T_1T_2) have been investigated by quantum chemistry and MC-TST method. The mechanism for the reaction between HO_2 and n-$C_3H_7O_2$ radical on both singlet and triplet potential energy surfaces mainly includes hydrogen abstraction and addition–elimination mechanisms. The energy barriers show the main products are $C_3H_7O_2H$ and $^3O_2$ on the triplet potential energy surface *via* the hydrogen abstraction mechanism. In addition, the rate constants of $HO_2 + n$-$C_3H_7O_2$ reaction were further studied over the temperature range of 238–398 K which show a negative temperature dependent. The kinetic calculations indicate that the formation of $C_3H_7O_2H + {}^3O_2$ channel is most kinetically favorable since that the rate constant of which is at least four orders of magnitude larger than that of the other channels at the studied temperature range. The calculated rate constant for $HO_2 + n$-$C_3H_7O_2$ reaction is predicted to be 6.27×10^{-12} cm^3 per molecule per s at 298 K, which match good with the results from SAR analysis.[10] The

theoretical results can be helpful to deeply understand the chemical behaviors of HO_2 + n-$C_3H_7O_2$ reaction.

Conflicts of interest

There are no conflicts to declare.

Acknowledgements

We would like to thank financial support from the National Natural Science Foundation of China (91544228, 41605102, 21876177, and 41575125), the National Key Research and Development Program of China (2016YFC0202205, 2017YFC0209401), the Youth Innovation Promotion Association CAS (2019439), and the Science and Technology Foundation of Guizhou Province, China ([2019]5648 and [2018]1080).

References

1 H. B. Singh, D. O'Hara, D. Herlth, W. Sachse, D. R. Blake, J. D. Bradshaw, M. Kanakidou and P. J. Crutzen, *J. Geophys. Res.*, 1994, **99**, 1805–1819.
2 R. Atkinson, *J. Phys. Chem. Ref. Data*, 1997, **26**, 215–290.
3 C. M. Rosado-Reyes and J. S. Francisco, *J. Geophys. Res.*, 2007, **112**, D14310.
4 L. K. Huynh, H.-H. Carstensen and A. M. Dean, *J. Phys. Chem. A*, 2010, **114**, 6594–6607.
5 S. S. Merchant, C. F. Goldsmith, A. G. Vandeputte, M. P. Burke, S. J. Klippenstein and W. H. Green, *Combust. Flame*, 2015, **162**, 3658–3673.
6 C. F. Goldsmith, W. H. Green and S. J. Klippenstein, *J. Phys. Chem. A*, 2012, **116**, 3325–3346.
7 G. S. Tyndall, R. A. Cox, C. Granier, R. Lesclaux, G. K. Moortgat, M. J. Pilling, A. R. Ravishankara and T. J. Wallington, *J. Geophys. Res.: Atmos.*, 2001, **106**, 12157–12182.
8 J. J. Orlando and G. S. Tyndall, *Chem. Rev.*, 2003, **103**, 4657–4689.
9 A. A. Boyd, P.-M. Flaud, N. Daugey and R. Lesclaux, *J. Phys. Chem. A*, 2003, **107**, 818–821.
10 H. Hou, J. Li, X. Song and B. Wang, *J. Phys. Chem. A*, 2005, **109**, 11206–11212.
11 A. S. Hasson, G. S. Tyndall and J. J. Orlando, *J. Phys. Chem. A*, 2004, **108**, 5979–5989.
12 Y. Shao, H. Hou and B. Wang, *Phys. Chem. Chem. Phys.*, 2014, **16**, 22805–22814.
13 G. M. P. Just, P. Rupper, T. A. Miller and W. L. Meerts, *Phys. Chem. Chem. Phys.*, 2010, **12**, 4773–4782.
14 S. J. Zalyubovsky, B. G. Glover, T. A. Miller, C. Hayes, J. K. Merle and C. M. Hadad, *J. Phys. Chem. A*, 2005, **109**, 1308–1315.
15 G. Tarczay, S. J. Zalyubovsky and T. A. Miller, *Chem. Phys. Lett.*, 2005, **406**, 81–89.
16 A. D. Becke, *J. Chem. Phys.*, 1993, **98**, 5648–5652.
17 C. Lee, W. Yang and R. G. Parr, *Phys. Rev. B: Condens. Matter Mater. Phys.*, 1988, **37**, 785–789.
18 C. Gonzalez and H. B. Schlegel, *J. Chem. Phys.*, 1989, **90**, 2154–2161.
19 C. Gonzalez and H. B. Schlegel, *J. Phys. Chem.*, 1990, **94**, 5523–5527.
20 K. Fukui, *Acc. Chem. Res.*, 1981, **14**, 363–368.
21 M. Page and J. W. McIver Jr, *J. Chem. Phys.*, 1988, **88**, 922–935.
22 K. Raghavachari, G. W. Trucks, J. A. Pople and M. Head-gordon, *Chem. Phys. Lett.*, 1989, **157**, 479–483.
23 J. C. Rienstra-Kiracofe, W. D. Allen and H. F. Schaefer, *J. Phys. Chem. A*, 2000, **104**, 9823–9840.
24 B. Long, X. Tan, Z. Long, Y. Wang, D.-s. Ren and W. Zhang, *J. Phys. Chem. A*, 2011, **115**, 6559–6567.
25 B. Long, J. L. Bao and D. G. Truhlar, *J. Am. Chem. Soc.*, 2016, **138**, 14409–14422.
26 B. Long, J. L. Bao and D. G. Truhlar, *J. Am. Chem. Soc.*, 2019, **141**, 611–617.
27 M. J. Frisch, G. W. Trucks, H. B. Schlegel, G. E. Scuseria, M. A. Robb, J. R. Cheeseman, G. Scalmani, V. Barone, B. Mennucci, G. A. Petersson, H. Nakatsuji, M. Caricato, X. Li, H. P. Hratchian, A. F. Izmaylov, J. Bloino, G. Zheng, J. L. Sonnenberg, M. Hada, M. Ehara, K. Toyota, R. Fukuda, J. Hasegawa, M. Ishida, T. Nakajima, Y. Honda, O. Kitao, H. Nakai, T. Vreven, J. A. Montgomery Jr, J. E. Peralta, F. Ogliaro, M. Bearpark, J. J. Heyd, E. Brothers, K. N. Kudin, V. N. Staroverov, R. Kobayashi, J. Normand, K. Raghavachari, A. Rendell, J. C. Burant, S. S. Iyengar, J. Tomasi, M. Cossi, N. Rega, J. M. Millam, M. Klene, J. E. Knox, J. B. Cross, V. Bakken, C. Adamo, J. Jaramillo, R. Gomperts, R. E. Stratmann, O. Yazyev, A. J. Austin, R. Cammi, C. Pomelli, J. W. Ochterski, R. L. Martin, K. Morokuma, V. G. Zakrzewski, G. A. Voth, P. Salvador, J. J. Dannenberg, S. Dapprich, A. D. Daniels, Ö. Farkas, J. B. Foresman, J. V. Ortiz, J. Cioslowski and D. J. Fox, *Gaussian 09, Revision A.02,* Gaussian, Inc., Wallingford CT, 2009.
28 H.-J. Werner, P. J. Knowles, G. Knizia, F. R. Manby and M. Schütz, *Wiley Interdiscip. Rev.: Comput. Mol. Sci.*, 2012, **2**, 242–253.
29 H.-J. Werner, P. J. Knowles and G. Knizia, *et al.*, *MOLPRO, version 2010.1, a package of ab initio program*, 2010.
30 K. H. Moller, R. V. Otkjaer, N. Hyttinen, T. Kurten and H. G. Kjaergaard, *J. Phys. Chem. A*, 2016, **120**, 10072–10087.
31 L. Vereecken and J. Peeters, *J. Chem. Phys.*, 2003, **119**, 5159–5170.
32 J. Peeters, J. F. Muller, T. Stavrakou and V. S. Nguyen, *J. Phys. Chem. A*, 2014, **118**, 8625–8643.
33 H. Eyring, *Chem. Rev.*, 1935, **17**, 65–77.
34 H. Eyring, *J. Chem. Phys.*, 1935, **3**, 107–115.
35 M. G. Evans and M. Polanyi, *Trans. Faraday Soc.*, 1935, **31**, 875–894.
36 D. G. Truhlar, B. C. Garrett and S. J. Klippenstein, *J. Phys. Chem.*, 1996, **100**, 12771–12800.
37 C. Eckart, *Phys. Rev.*, 1930, **35**, 1303–1309.

